

Experimental Demonstration of Swift Analytical Universal Control Over Nearby Transitions

Yue Li^{1,2,§}, Zhi-Cheng He^{3,§}, Xinxing Yuan^{1,2,§}, Mengxiang Zhang^{1,2}, Chang Liu^{1,2},
Yi-Xuan Wu³, Mingdong Zhu^{1,2}, Xi Qin^{1,2,4}, Zheng-Yuan Xue^{3,5,*}, Yiheng Lin^{1,2,4,†} and
Jiangfeng Du^{1,2,4,‡}


¹CAS Key Laboratory of Microscale Magnetic Resonance and School of Physical Sciences, University of Science and Technology of China, Hefei 230026, China

²CAS Center for Excellence in Quantum Information and Quantum Physics, University of Science and Technology of China, Hefei 230026, China

³Guangdong Provincial Key Laboratory of Quantum Engineering and Quantum Materials, and School of Physics and Telecommunication Engineering, South China Normal University, Guangzhou 510006, China

⁴Hefei National Laboratory, University of Science and Technology of China, Hefei 230088, China

⁵Guangdong-Hong Kong Joint Laboratory of Quantum Matter, and Frontier Research Institute for Physics, South China Normal University, Guangzhou 510006, China

 (Received 16 January 2022; revised 10 July 2022; accepted 5 August 2022; published 19 September 2022)

Along with the scaling of dimensions in quantum systems, transitions between the system's energy levels would become close in frequency, which are conventionally resolved by weak and lengthy pulses. Here, we extend and experimentally demonstrate analytically based swift quantum control techniques on a four-level trapped ion system, where we perform individual or simultaneous control over two pairs of spectrally nearby transitions with tailored time-varied drive, achieving operational fidelities ranging from 99.2(3)% to 99.6(3)%. We achieve approximately an order of magnitude speed up compared with the case of a weak square pulse for a general control. Therefore, our demonstration may be beneficial to a broad range of quantum systems with crowded spectrum, for spectroscopy, quantum information processing, and quantum simulation.

DOI: [10.1103/PhysRevApplied.18.034047](https://doi.org/10.1103/PhysRevApplied.18.034047)

I. INTRODUCTION

Despite frequent utilization of two-level systems for many quantum enhanced applications, most practical systems are intrinsically of many levels in nature, e.g., for coherent quantum control in three-level systems [1–7]. Besides, for applications with quantum many-body systems, such as high-sensitivity precision measurements [8], large-scale quantum computation [9], and simulation of quantum many-body systems [10], either more qubits or larger internal complexities must be involved, and then the energy or associated frequency spectrum would become crowded. In these cases, spectrally resolving a transition with an external drive field for high-fidelity manipulation would become difficult, which may limit the scalability of quantum systems, and may hinder large-scale quantum tasks where precise quantum control over individual transition is required.

One straightforward solution for this limitation is to narrow the range of Fourier frequency components from the pulse of the drive field, for example, to apply smooth-shaped pulses [11–15] and using narrow linewidth transitions [16]. Frequency shifts to the nearby transition may also come into play, which could be compensated with a careful choice of parameters [17]. However, in general cases, a desired transition rate determines the minimum temporal integral of pulse strength, i.e., “pulse area,” and the lower field strength in turn results in longer pulse duration, leaving the control vulnerable to frequency drifts, decoherence, or limiting the number of operations in given finite coherence times. Meanwhile, insufficiently weak pulse strength would create unwanted transition in the adjacent spectral line, giving rise to a population leakage or cross-talk error in the control.

To tackle the problem of spectral crowding while keeping the operation fast, one idea is to abandon the assumption that the unwanted nearby transitions remain without being driven, but rather allowing a controlled evolution where the overall desired operation is reached at the end of the drive pulse. With high enough drive bandwidth, one can design square pulses with proper duration and

* zyxue83@163.com

† yiheng@ustc.edu.cn

‡ djf@ustc.edu.cn

§ All authors contributed equally.

strength to obtain the desired rotation on one transition while leaving the nearby transition intact at the end of the pulse. Such schemes require fixed drive strength to avoid the dynamical rotation axis for the detuned transition and, thus, are not applicable for techniques with intensity modulation and shaping, which are widely used for high-fidelity quantum manipulations. Or, in general cases, one can directly numerically search for the desired pulse shape with optimal control techniques [18–26], and, thus, an overall operation close enough to the target one can be obtained. However, for the numerical pulse shaping, it can only be done in a case-by-case way, and only one certain shape can be obtained under a particular set of conditions. Besides, due to the piecewise constant control ansatz, the complex numerical shape may be inaccurate in cases of bounded bandwidth. Perturbative methods including derivative removal by adiabatic gate [27] and its enhancement by the weak anharmonicity with average Hamiltonian method [28–30] are used to reduce leakage for crowded spectrum of qubit frequency separation.

On the other hand, for two-level quantum systems, the analytic solution for detuned single or multiple axes driving become available [31–33]. This brings an opportunity to better understand the underlying physics, and converting a full numerical optimization to a parametric boundary problem, where a series of solutions can be obtained when boundary conditions are met. Thus, one has the additional freedom to incorporate various pulse-shaping techniques, and find experimentally friendly simple pulse solutions. We note that this analytic solution can be extended to drive desired transitions in multilevel quantum systems, while leaving adjacent transitions intact. Therefore, such a technique can go beyond addressing a certain transition, and can be tailored to simultaneously drive nearby transitions. The combination of individual and simultaneous control would lead to the capability of arbitrary manipulations in the nearby transitions, and may assist in quantum logic operations on multilevel systems [13,34–40], leading to universal quantum control for both subspaces. Remarkably, as this technique removes the weak drive limitation, it might be also useful for spectroscopy, where a faster probe to obtain more information might be possible.

Here, we extend these analytical-based swift quantum control techniques to a four-level system, where individual or simultaneous quantum control over the two pairs of levels can be effectively obtained. We then experimentally demonstrate individual operation where a transition is driven while the other is intact, and simultaneous operations where quantum phase and Hadamard gate operations are performed on both transitions. We achieve operation fidelities ranging from 99.2(3)% to 99.6(3)%, limited by decoherence of the quantum system and experimental imperfections.

II. SWIFT ANALYTIC-BASED CONTROL

We firstly extend the previous two-level schemes [31–33] to the case of four levels $\{|1\rangle, |2\rangle, |3\rangle, |4\rangle\}$, forming two pairs of nearby transitions, as shown in Fig. 1(a), to implement a fast, high-fidelity universal control over the two transitions. Labeling the transition frequency between $|i\rangle \leftrightarrow |j\rangle$ as ω_{ij} , when the transition with ω_{34} is driven resonantly by an external field with time-varied Rabi rate Ω , the transition with ω_{12} is driven simultaneously by the same field with Rabi rate Ω' with detuning Δ from resonance. Here we consider the case that $\Omega \sim \Omega'$ and with a fixed ratio; the transition frequencies across the two pairs $\{|1\rangle, |2\rangle\} \leftrightarrow \{|3\rangle, |4\rangle\}$ are much larger than ω_{12} or ω_{34} , thus, we can limit our discussion within each pair. In the rotating framework, we obtain the interacting Hamiltonian as

$$H(t) = \frac{1}{2} \begin{pmatrix} \Delta & \Omega'(t)e^{-i\varphi} & 0 & 0 \\ \Omega'(t)e^{i\varphi} & -\Delta & 0 & 0 \\ 0 & 0 & 0 & \Omega(t)e^{-i\varphi} \\ 0 & 0 & \Omega(t)e^{i\varphi} & 0 \end{pmatrix}, \quad (1)$$

where φ is the phase of the drive field and we set $\hbar = 1$. Thus, the nearby small detuned transition will be excited unintentionally, leading to phase and leakage errors, i.e., the so-called spectral crowding problem. The trivial way to deal with the problem is to drive the target transitions with a lower Rabi rate, i.e., $\max\{\Omega, \Omega'\}/\Delta \ll 1$, typically with $\max\{\Omega, \Omega'\}/\Delta \lesssim 0.1$ for a general control. However, lower Rabi rates lead to a longer control time and a fewer

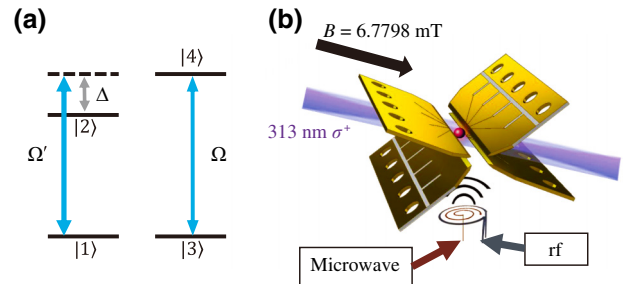


FIG. 1. Illustration of the scheme and the experimental setup. (a) A four-level system with two pairs of closely spaced transitions is considered, where a small detuning Δ exists between transitions with respective resonant frequency of ω_{12} and ω_{34} . With the same external drive, Rabi rates for these transitions are denoted as Ω' and Ω , respectively. (b) A trapped-ion system with a ${}^9\text{Be}^+$ ion trapped in a linear Paul trap. A series of controlled 313 nm laser beams with σ^+ polarization along the magnetic field direction is applied for Doppler cooling, optical pumping, and resonant fluorescence detection. The magnetic field is provided by a set of $\text{Sm}_2\text{Co}_{17}$ permanent magnets forming a magnetic field of 6.7798 mT at the ion. Two impedance matched antennas are set under the trap, where one is for rf drive and the other is for microwave drive.

number of control pulses within the coherence times. As we analyze and experimentally demonstrate below, the time-dependent control in this work would enable individual or simultaneous control of both transitions, even with $\max\{\Omega, \Omega'\}/\Delta \sim 1$, thus giving approximately an order of magnitude speed up. Actually, we do not apply any restriction on the value of $\max\{\Omega, \Omega'\}/\Delta$ and, thus, it is also applicable to the case of $\max\{\Omega, \Omega'\}/\Delta \gg 1$.

To illustrate the idea for swift analytic-based control, we consider the general evolution operator of Hamiltonian in Eq. (1) with a duration $[0, T]$ as

$$\begin{pmatrix} U'(t) & 0 \\ 0 & U(t) \end{pmatrix}, \quad (2)$$

where $U(t)$ and $U'(t)$ are the evolution operator for the resonant and detuned subspace, respectively. To obtain precise control over the transitions, we need to obtain target dynamics for both subspaces, preferably beyond the weak drive limit. While the evolution in the resonant subspace is related to the pulse area and phase given by $\Omega(t)e^{i\varphi}$ in Eq. (1) in a straightforward way, the complex dynamics of the detuned subspace can be obtained, by extending Refs. [31–33].

The Hamiltonian for the two-level subspace that is driven by a classical field in a detuned way is

$$H = \frac{1}{2} \begin{pmatrix} \Delta & \Omega'(t)e^{-i\varphi} \\ \Omega'(t)e^{i\varphi} & -\Delta \end{pmatrix}, \quad (3)$$

where Δ is the detuning between the transition frequency and the driving field frequency, with $\Omega'(t)$ and φ being the amplitude and phase of the driving field, respectively. To obtain the solution, we first apply a $\pi/2$ rotation around the vertical axis of the φ axis in the x - y plane, denoted as U_R , and the Hamiltonian will be changed to

$$H_R = \frac{1}{2} \begin{pmatrix} \Omega'(t) & -\Delta e^{-i\varphi} \\ -\Delta e^{i\varphi} & -\Omega'(t) \end{pmatrix}. \quad (4)$$

Generally, the corresponding time evolution operator for the above Hamiltonian can be written as

$$U_0 = \begin{pmatrix} u_{11}(t) & -u_{21}^*(t) \\ u_{21}(t) & u_{11}^*(t) \end{pmatrix}, \quad (5)$$

with $|u_{11}(t)|^2 + |u_{21}(t)|^2 = 1$. In the rotating framework of $S(t) = \exp\left[-(i/2) \int_0^t \Omega'(t') dt' \sigma_z\right]$, the Schrödinger equation of the evolution operator $i\dot{U}_0(t) = HU_0(t)$ will

change to

$$\dot{v}_{11}(t) = i\frac{\Delta}{2} e^{i\alpha(t)} v_{21}(t), \quad (6a)$$

$$\dot{v}_{21}(t) = i\frac{\Delta}{2} e^{-i\alpha(t)} v_{11}(t), \quad (6b)$$

where

$$v_{11}(t) = \exp\left(i\frac{1}{2} \int_0^t \Omega' dt'\right) u_{11}(t),$$

$$v_{21}(t) = \exp\left(-i\frac{1}{2} \int_0^t \Omega' dt'\right) u_{21}(t),$$

and $\alpha(t) = \int_0^t \Omega'(t') dt' - \varphi$. The above relation can lead to

$$\frac{v_{11} \dot{v}_{21}}{v_{11} v_{21}} = -\frac{\Delta^2}{4}. \quad (7)$$

We further separate the left part as two different equations of v_{11} , v_{21} , and similarly, with respect to the Schrödinger equation form, the right part would also be separated with a complex parameter $\kappa(t)$, i.e., $i(\Delta/2)e^{\pm\kappa(t)}$. By solving these separated differential equations, we get

$$v_{11} = e^{i\theta_1} \exp\left[i \int_0^t \frac{\Delta}{2} e^{\kappa(t')} dt'\right], \quad (8a)$$

$$v_{21} = e^{i\theta_2} \exp\left[i \int_0^t \frac{\Delta}{2} e^{-\kappa(t')} dt'\right], \quad (8b)$$

where the complex function $\kappa(t)$ is unknown yet. Here θ_1 and θ_2 are constant phases which are hidden in the derivation. Meanwhile, we can also denote $\alpha(t)$ in terms of $\kappa(t)$ as

$$\alpha(t) = -i\kappa(t) + \theta - \int_0^t \Delta \sinh \kappa(t') dt', \quad (9)$$

where $\theta = \theta_1 - \theta_2$. As Δ and φ are real, the function $\alpha(t)$ defined by them also should be a real function, which allows us to derive the relationship between the real and imaginary parts of $\kappa(t)$. Thus, the real and imaginary parts of $\kappa(t)$ are obtained as

$$\kappa_R(t) = \ln\{-\tan[\chi(t) + C]\}, \quad (10a)$$

$$\kappa_I(t) = \arcsin \frac{2\dot{\chi}(t)}{\Delta}, \quad (10b)$$

where $\chi(t) = \frac{1}{2} \int_0^t \Delta \sin \kappa_I(t') dt'$, and C is an integral constant.

By applying $S^\dagger(t)$, and returning back to the picture with respect to H_R , then, the evolution operator is calculated as

$$U_0 = \begin{pmatrix} e^{i\xi_-(t)} \cos \zeta(t) & -e^{-i(\xi_+(t)+\varphi)} \sin \zeta(t) \\ e^{i(\xi_+(t)+\varphi)} \sin \zeta(t) & e^{-i\xi_-(t)} \cos \zeta(t) \end{pmatrix}, \quad (11)$$

where $\zeta(t) = \chi(t) + C$ and

$$\xi_{\pm}(t) = \int_0^t \frac{\Delta}{2} \sqrt{1 - \left[\frac{2\dot{\zeta}(t')}{\Delta} \right]^2} \csc[2\zeta(t')] dt' \pm \frac{1}{2} \arcsin \frac{2\dot{\zeta}(t)}{\Delta}.$$

Here, we also set $\theta = \varphi$ for simplicity, but in general, it can be arbitrary, as we discuss below. Besides, we also set $\dot{\zeta}(0) = \dot{\zeta}(T) = 0$ to simplify our calculation. Then the amplitude of the driving field can be obtained as

$$\Omega'(t) = \frac{2\ddot{\zeta}(t)}{\Delta \sqrt{1 - [2\dot{\zeta}(t)/\Delta]^2}} - \Delta \sqrt{1 - \left[\frac{2\dot{\zeta}(t)}{\Delta} \right]^2} \cot[2\zeta(t)]. \quad (12)$$

Because of the practical restriction of the pulse shape, the function $\zeta(t)$ should be chosen so that $\cot[2\zeta(t)]$ and $\sqrt{1 - [2\dot{\zeta}(t)/\Delta]^2}$ are finite. Besides, to be more experimentally friendly, we also set $\Omega'(0) = \Omega'(T) = 0$.

Furthermore, considering the boundary condition $U_C(0) = I$ must be met for any C , we set the operator with the form of

$$U_C(t) = U_0(t) \cdot U_0^\dagger(0). \quad (13)$$

Note that, the unknown constant phases θ_1 and θ_2 are canceled themselves in the calculation leading to the operator U_C under this assumption, as verified by our numerical simulation and experiment. Finally, turning back to the original frame, the analytical solution of the time evolution operator is

$$U'(t) = U_R U_C(t) U_R^\dagger, \quad (14)$$

where U_R is

$$U_R = \exp \left[-i \frac{\pi}{4} \begin{pmatrix} 0 & e^{-i[\varphi+(\pi/2)]} \\ e^{i[\varphi+(\pi/2)]} & 0 \end{pmatrix} \right]. \quad (15)$$

This analytic solution allows us to achieve any SU(2) matrix, and the required $\Omega'(t)$ is determined by $\zeta(t)$ and Δ as shown in Eq. (12). Thus, it is possible to design $\zeta(t)$ for arbitrary control in the detuned subspace. For the resonant subspace, given a fixed value of Ω/Ω' , Eq. (12) leads

to a waveform of $\Omega(t)$ for a controlled rotation; concatenated segments with varied φ give arbitrary control. To obtain $\zeta(t)$, we can further decompose $\zeta(t)$ into a weighted sum of analytic functions, e.g., sinusoidal functions, with a period equal to the total operation time T , and we can numerically find proper weights to obtain a required overall operation at T , under further constrains of $\dot{\zeta}(t)^2/\Delta^2 < 1$ and $\cot[2\zeta(t)]$ being finite. Thus, a desired operation can be obtained up to numerical precision, whose error is negligible comparing to experimental imperfections. In practice, we set $T \sim 1.4\pi/\Delta$, then $\dot{\zeta}(t)$ and $\ddot{\zeta}(t)$ are of the order of Δ and Δ^2 , respectively. Thus, in general, the two terms in Eq. (12) are both of the order of Δ and are not canceled with each other, so that the average of the Rabi rates can be roughly of the order of Δ , and the operation time is much shorter than the weak driven case.

III. EXPERIMENTAL SETUP

In our experiment we trap a $^9\text{Be}^+$ ion in a linear Paul trap [41], as shown in Fig. 1(b), and the desired Hilbert space is defined within the $2s^2S_{1/2}$ hyperfine states $|F, m_F\rangle$ of the ion, with $|1\rangle \equiv |1, 1\rangle$, $|2\rangle \equiv |1, 0\rangle$, $|3\rangle \equiv |2, 1\rangle$ and $|4\rangle \equiv |2, 0\rangle$. Applying an ambient magnetic field at 6.7798 mT, we have $\omega_{12} = 2\pi \times 48.798$ MHz, $\omega_{34} = 2\pi \times 48.879$ MHz, $\Delta \equiv \omega_{34} - \omega_{12} = 2\pi \times 81$ kHz, and $\omega_{13} = 2\pi \times 1.16$ GHz. We apply rf fields driving transitions $|1\rangle \leftrightarrow |2\rangle$ and $|3\rangle \leftrightarrow |4\rangle$. Radio frequencies are generated by an arbitrary wave generator (AWG) with a power amplifier, see Appendix A for details, and, thus, can be fully controlled by programming the AWG. When we drive the transition $|3\rangle \leftrightarrow |4\rangle$ on resonance with Rabi rate Ω , the transition $|1\rangle \leftrightarrow |2\rangle$ is also driven with Rabi rate Ω' and a detuning Δ , thus implementing the Hamiltonian in Eq. (1). The Rabi rate ratio Ω/Ω' is experimentally measured to be 1.7, and remains fixed throughout the experiment since it depends on the coupling constants. To assist state preparation and detection, we also apply microwave fields to a separate antenna, as shown in Fig. 1(b), sourced by a power amplified frequency-doubled direct digital synthesizer.

IV. INDIVIDUAL CONTROL

As a demonstration of individual control over one of the two closely spaced transitions, while leaving the other intact, we perform a simultaneous operation on both pairs of transitions with $U(T) = X$ and $U'(T) = I$ ($\varphi = 0$), where X is a Pauli operator and I is an identity operation. According to Eq. (12), we can obtain $\Omega(t)$ from $\zeta(t)$ and Δ , where we set

$$\zeta(t) = \phi_Z + \sum_{n=3}^5 A_n \sin^n \left(\pi \frac{t}{T} \right), \quad (16)$$

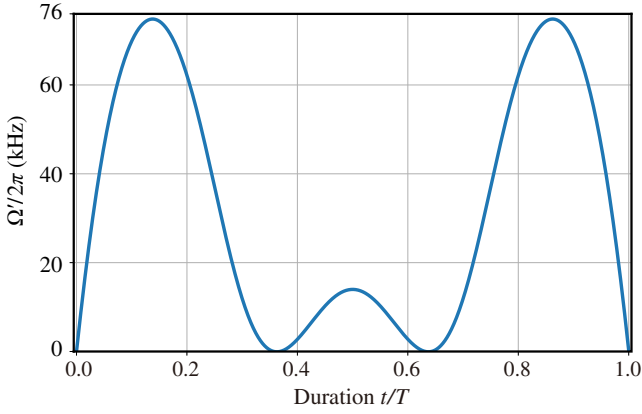


FIG. 2. A typical waveform designed for individual control with parameter $A_3 = -0.793$, $A_4 = 0.464$, $A_5 = -0.085$, and gate time $T = 8.88 \mu\text{s}$.

with $\phi_Z = \pi/4$, leading to $\dot{\zeta}(0) = \dot{\zeta}(T) = \ddot{\zeta}(0) = \ddot{\zeta}(T) = 0$; thus, $\xi_+(0) = \xi_-(0) = 0$, $\xi_+(T) = \xi_-(T)$ and $\Omega(0) = \Omega(T) = 0$. When we design a specific waveform, we can set the boundary conditions and find parameters by numerical optimization with the trust region dogleg method [42]. By setting $T = 8.88 \mu\text{s}$ for $\Delta = 2\pi \times 81$ kHz and with numerical optimization, we obtain $A_{3,4,5} = \{-0.793, 0.464, -0.085\}$, respectively, giving $\xi_+(T) = \xi_-(T) = 2\pi$, and the resulting pulse shape is shown in Fig. 2. Thus, the average of Rabi rates $\bar{\Omega} = 2\pi \times 56$ kHz and $\bar{\Omega}' = 2\pi \times 33$ kHz, comparable to Δ . The quantum dynamics is shown in Fig. 3(a), where the solid lines are obtained by theoretical simulation while the points are the experimental results. The quantum process can be described by $\rho_{\text{out}} = \sum_{j,k} E_j \rho_{\text{in}} E_k^\dagger \chi_{jk}$, where ρ_{in} is the density matrix of the initial state, ρ_{out} is the density matrix of the state after the process, $E_{j,k} \in \{I, X, Y, Z\}$ are basis operators, I is the identity operation, and X , Y , and Z represent Pauli operators. Thus, the matrix χ uniquely represents the process. To estimate the components of χ for the operation, we perform process tomography [45–47], where we initialize the ion to various states, apply the operation, and measure the outcome. For example, to measure components of U , we first apply Doppler cooling, optical pumping with 313 nm laser pulses to prepare $|2, 2\rangle$ state, and apply resonant microwave π or $\pi/2$ pulses to transfer to states of $|3\rangle$, $|4\rangle$, $(|3\rangle + |4\rangle)/\sqrt{2}$ and $(|3\rangle + i|4\rangle)/\sqrt{2}$, respectively. After applying the operation, we map one state in the pair to $|1, -1\rangle$ and the other to $|2, 2\rangle$ by a series of microwave pulses, followed by resonant fluorescent measurement by driving $|2, 2\rangle$ to $2p^2P_{3/2}$ for $400 \mu\text{s}$, while the $|1, -1\rangle$ state is out of resonance and appears dark. We typically collect on average 25 counts for $|2, 2\rangle$ and less than 1 count for dark states. We perform each measurement for 1000 trials to reconstruct ρ_{out} by maximum likelihood state tomography [14,43,44], and from

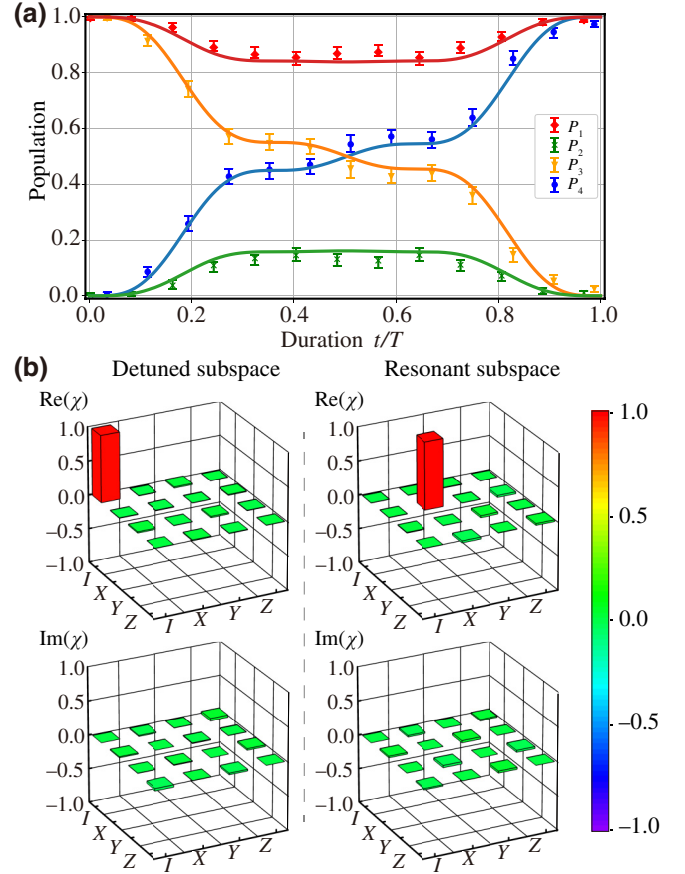


FIG. 3. Performance of individual control. (a) The population dynamics of P_i for each basis state $|i\rangle$ under the applied control pulse. The solid lines are obtained from numerical simulation without considering experimental imperfections, overlapped with experimentally obtained populations. Each measurement is obtained from a maximum likelihood estimation with 1000 trials. Error bars are obtained from bootstrap resampling with 95% confidence interval [14,43,44]. (b) Process matrices (χ) for the individual control, obtained in a separate experimental run from (a). The height of the bars represents the amplitude of the matrix components, with the real and imaginary parts shown. Ideally, only the II element for detuned space and the XX element for resonant space of the process matrix are unity and all other components are zero. See Appendix B for the detailed data.

which we further obtain the process matrix components, as shown in Fig. 3(b). A similar procedure is repeated to measure components of $U^\dagger(T)$. We obtain process fidelity [45,48] $F_U = 99.5(4)\%$ and $F_{U^\dagger} = 99.6(3)\%$, respectively, through the definition of

$$F = \frac{|\text{Tr}(\chi_{\text{exp}} \chi_{\text{ideal}})|}{\sqrt{\text{Tr}(\chi_{\text{exp}} \chi_{\text{exp}}^\dagger) \text{Tr}(\chi_{\text{ideal}} \chi_{\text{ideal}}^\dagger)}}, \quad (17)$$

where χ_{ideal} is the ideal process matrix for the corresponding operation and χ_{exp} is the measured one. In our experiment, the measured coherence times for the resonant and

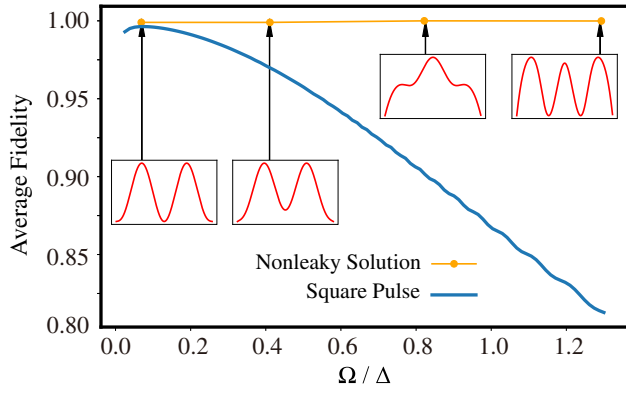


FIG. 4. Simulation of the average gate fidelity with a dephasing rate of $\Delta/40$, and $\Omega/\Omega' = 1.7$, to match with realistic experimental conditions. Here we compare our analytical solution-based pulse with the direct square pulse driving. With increasing Ω/Δ , high fidelity ($> 99.8\%$) can be maintained for the analytical-based solution, showing the nonleaky feature of such a method, while the fidelity for a square pulse deteriorates beyond the weak-driving limit. The inset figures are typical waveforms at different ratios.

detuned subspaces are approximately 1.9 ms and 1.1 ms, respectively, with a Ramsey-type experiment, which will contribute up to approximately 0.2% operation infidelity. Experimentally, we also observe fast drifts of the ambient magnetic field after each calibration, which, together with other unknown ones, we attribute as other possible error sources. Finally, to compare with the case of a weak square pulse, we perform a numerical simulation as shown in Fig. 4. Given a realistic decoherence of $\Delta/40$ and $\Omega/\Omega' = 1.7$ as in the experiment and without further imperfections, the optimal control fidelity with a square pulse is reached at $\Omega/\Delta \sim 0.08$, while for our implementation, a similar fidelity can be achieved at $\Omega/\Delta \sim 0.7$ and, thus, decrease the required operation time by approximately an order of magnitude.

V. UNIVERSAL QUANTUM CONTROL

We next demonstrate simultaneous quantum control over both pairs of transitions. For the Hamiltonian in Eq. (1), the resonant subspace is a simple Rabi control, which can be used to obtain an arbitrary quantum gate with no limitation on the waveform detail of the drive. Thus, providing Eq. (12) is met for the waveform in the detuned subspace, we also arrive at the arbitrary control over this subspace as in Eq. (13). Therefore, besides the individual control, we also present how to implement simultaneous quantum gates on both subspaces, represented by the S gate, T gate, and Hadamard (H) gate, as detailed below. For a qubit system, these gates form a universal set of single-qubit gates.

In the case of the S gate, such an operation is a $\pi/4$ rotation around the σ_z axis in both detuned and resonant

subspace, i.e.,

$$U'(\tau) = \begin{pmatrix} e^{i(\pi/4)} & 0 \\ 0 & e^{-i(\pi/4)} \end{pmatrix}, \quad U(\tau) = \begin{pmatrix} e^{i(\pi/4)} & 0 \\ 0 & e^{-i(\pi/4)} \end{pmatrix}.$$

To implement this single-bit gate, we need two π pulses with different φ . In the resonant subspace, we set

$$\int_0^{\tau_1} \frac{1}{2} \Omega(t) dt = \frac{\pi}{2}, \quad \varphi_1 = 0, \quad (18a)$$

$$\int_{\tau_1}^{\tau_2} \frac{1}{2} \Omega(t) dt = \frac{\pi}{2}, \quad \varphi_2 = -\frac{\pi}{4}. \quad (18b)$$

So gate $U(\tau)$ is implemented. For the detuned subspace, recall the analytic solution, we find that the phase ξ in evolution operator is independent of φ of the drive field; thus, the phase ξ in these two pulses are actually equal, and the final operator is

$$\begin{pmatrix} e^{i2\xi} & 0 \\ 0 & e^{-i2\xi} \end{pmatrix}.$$

When $2\xi = \pi/4$, we implement the gate $U'(\tau)$, so S gates in two subspaces are obtained. The amplitudes for both steps of the waveform designed for the S gate are the same with $A_{3,4,5} = \{-0.259, -0.059, -0.093\}$ and $\tau_1 = \tau_2 = 10.39 \mu\text{s}$. As for the T gates, by setting $2\xi' = \pi/8$, they can be implemented in a similar way. The waveform parameters designed for the T gate are $A_{3,4,5} = \{-0.134, -0.077, -0.197\}$ and $\tau_1 = \tau_2 = 11.15 \mu\text{s}$.

We now consider the Hadamard (H) gate for both subspaces, that is,

$$U'(\tau) = \frac{1}{\sqrt{2}} \begin{pmatrix} 1 & 1 \\ 1 & -1 \end{pmatrix}, \quad U(\tau) = \frac{1}{\sqrt{2}} \begin{pmatrix} 1 & 1 \\ 1 & -1 \end{pmatrix}.$$

To implement the gate in resonant subspace, we decompose the H gate as $H = X \times \sqrt{Y}$, where X (Y) denote the Pauli matrix σ_x (σ_y), which could be obtained by a resonant pulse with different phase $\varphi = 0(\pi/2)$ with the pulse area being $\pi(\pi/2)$. Thus, we set

$$\int_0^{\tau_1} \Omega(t) dt = \pi/2, \quad \varphi_1 = \pi/2, \quad (19a)$$

$$\int_{\tau_1}^{\tau_2} \Omega(t) dt = \pi, \quad \varphi_2 = 0. \quad (19b)$$

For the detuned subspace, we implement an identity in the first part of evolution, and a H gate for the second part. The corresponding restriction of parameter in the second part is $\zeta(\tau_1) = \zeta(\tau_2) = 3\pi/8$, and the second part of the waveform is designed with parameters $A_{3,4,5} = \{-1.093, 0.747, -0.360\}$ and $\tau_2 = 16.49 \mu\text{s}$. Similarly to before, the H gate could be implemented with an accurately calculated A_n with $\xi = \pi/2$.

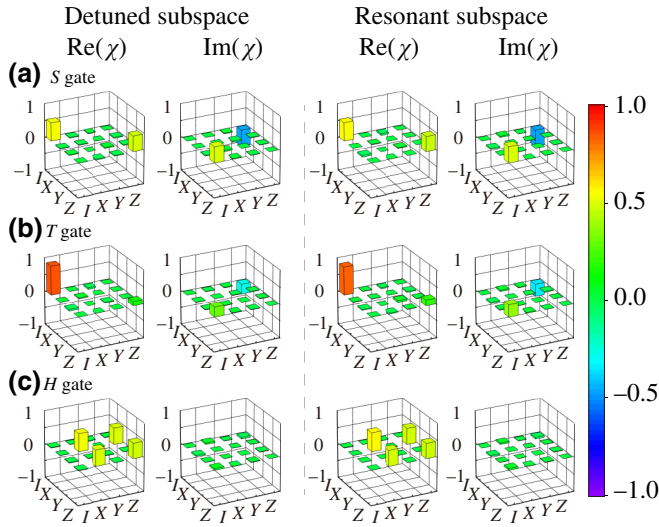


FIG. 5. Bar chart for the process matrices of simultaneous control for both transitions. Despite the fact that a small but non-negligible detuning between the two subspaces exists, the same gate can be achieved by a time-dependent drive, for (a) S gate, (b) T gate, and (c) H gate, with the real and imaginary components shown. See Appendix C for the detailed data.

We design waveforms with gate time $\tau_{S,T,H} = \{20.77, 22.29, 25.37\}$ μs respectively for each gate, similar to the process above and perform process tomography. The process matrices are shown in Fig. 5, with process fidelity $F'_S = 99.4(3)\%$, $F_S = 99.4(3)\%$, $F'_T = 99.3(3)\%$, $F_T = 99.4(4)\%$, $F'_H = 99.2(2)\%$, and $F_H = 99.2(3)\%$, where $F'_{S/T/H}$ and $F_{S/T/H}$ correspond to S , T , and H gates on the detuned and resonant transitions, respectively. We estimate the decoherence affects of the measured fidelity with a contribution up to 0.3%, 0.3%, and 0.4% for S , T , and H gates, respectively.

VI. CONCLUSIONS

In conclusion, we experimentally demonstrate quantum control over two pairs of nearby transitions with time-dependent pulses, where the waveform parameters can be readily obtained with the help of an analytical model. We demonstrate individual and simultaneous control of each pair of transitions, reaching a process fidelity up to 99.6(3)%. Our work can be extended to a range of systems. For example, in recent experiments with trapped molecular ions, adjacent transitions can be spaced on the order of kilohertz, rendering the transition pulse duration on the order of milliseconds with smooth edges [13]; and for a long ion chain, coupled motional modes can space below 10 kHz [34,40] and superconducting transmon qubits with weak anharmonic levels [35]. For future research, it might be interesting to enhance the robustness for the designed shaped pulses or even incorporate optimization requirements into the process of finding a target solution [49]. In

addition, as more levels may be involved for many-body or many-degree-of-freedom quantum systems, extending the current mathematical model to cover more levels that are closely spaced may be also of practical interest. On the other hand, our demonstration involves four levels orthogonal to each other, thus, some extension would be needed when the transitions involve a shared energy level, such as Λ -, V -, and ladder-type systems, possibly combining with the stimulated Raman adiabatic passage technique [2,3]. Regarding quantum sensing and metrology, this demonstration might be beneficial to vector magnetometry utilizing nitrogen-vacancy centers [50] to produce a fast probe driving nearby transitions corresponding to a few crystal orientations.

ACKNOWLEDGMENTS

We thank Pengfei Wang and Xinhua Peng for helpful discussions. We acknowledge support from the National Natural Science Foundation of China (Grants No. 92165206, No. 11974330, and No. 11874156), the Chinese Academy of Sciences (Grant No. XDC07000000), Innovation Program for Quantum Science and Technology (Grant No. 2021ZD0301603), Anhui Initiative in Quantum Information Technologies (Grant No. AHY050000), the Fundamental Research Funds for the Central Universities, and Hefei Comprehensive National Science Center.

APPENDIX A: DETAILS OF EXPERIMENT HARDWARE

We use commercial 313 nm laser sources from Precilasers Co. Ltd. (YEFL-FHG-313-0.3-CW), frequency locked to reference spectral lines of molecular iodine with a home-built saturation spectroscopy setup via the 626 nm monitor output. We use commercial AWG from Ciqtek (AWG4100). The AWG is triggered and synchronized with a home-developed board and user interface (based on and modified from [51]), which control direct digital synthesizer and transistor-transistor logic for other pulses and record photon counts during fluorescent detection. The maximum power we use for rf and microwave fields are 50 W and 30 W, respectively. We set two separate antennas for rf drive and microwave drive, about 2 cm away from the ion. The rf antenna has a shape of a coil with around a 3-cm diameter made from a single turn of copper wire. A 100-nH inductor and a 30-pF capacitor in parallel with the coil improve the coupling of the rf to the antenna. The microwave field is delivered through a twin spiral antenna with a diameter of around 3 cm.

APPENDIX B: EXPERIMENTAL RESULT FOR INDIVIDUAL CONTROL

The data of the χ matrix in each of the subspaces are

$$\text{Re}(\chi'_{\text{ID}}) = \begin{pmatrix} 0.997 & -0.008 & 0.019 & 0.005 \\ -0.010 & -0.010 & -0.005 & 0.013 \\ 0.019 & -0.005 & 0.020 & -0.008 \\ 0.005 & 0.013 & -0.008 & 0.004 \end{pmatrix}, \quad (\text{B1})$$

$$\text{Re}(\chi'_T) = \begin{pmatrix} 0.832 & 0.009 & -0.026 & -0.001 \\ 0.009 & -0.007 & 0.001 & -0.025 \\ -0.026 & 0.001 & 0.051 & 0.009 \\ -0.001 & -0.025 & 0.009 & 0.180 \end{pmatrix}, \quad (\text{C5})$$

$$\text{Im}(\chi'_{\text{ID}}) = \begin{pmatrix} 0.000 & 0.016 & -0.05 & -0.036 \\ -0.016 & 0.000 & 0.012 & 0.005 \\ 0.005 & -0.012 & 0.000 & -0.024 \\ 0.036 & -0.005 & 0.024 & 0.000 \end{pmatrix}, \quad (\text{B2})$$

$$\text{Im}(\chi'_T) = \begin{pmatrix} 0.000 & -0.035 & -0.023 & 0.363 \\ 0.035 & 0.000 & 0.006 & 0.023 \\ 0.023 & -0.006 & 0.000 & -0.004 \\ -0.363 & -0.023 & 0.004 & 0.000 \end{pmatrix}, \quad (\text{C6})$$

$$\text{Re}(\chi_{\text{ID}}) = \begin{pmatrix} -0.040 & 0.006 & 0.011 & 0.004 \\ 0.006 & 0.995 & -0.004 & -0.030 \\ 0.011 & -0.004 & 0.030 & 0.006 \\ 0.004 & -0.030 & 0.006 & 0.027 \end{pmatrix}, \quad (\text{B3})$$

$$\text{Re}(\chi_T) = \begin{pmatrix} 0.857 & 0.002 & -0.046 & -0.001 \\ 0.002 & 0.027 & 0.001 & -0.002 \\ -0.046 & 0.001 & -0.017 & 0.002 \\ -0.001 & -0.002 & 0.002 & 0.134 \end{pmatrix}, \quad (\text{C7})$$

$$\text{Im}(\chi_{\text{ID}}) = \begin{pmatrix} 0.000 & 0.024 & 0.002 & -0.019 \\ -0.024 & 0.000 & -0.033 & -0.002 \\ -0.002 & 0.034 & 0.000 & 0.030 \\ 0.020 & 0.002 & -0.030 & 0.000 \end{pmatrix}, \quad (\text{B4})$$

$$\text{Im}(\chi_T) = \begin{pmatrix} 0.000 & 0.008 & -0.015 & 0.294 \\ -0.008 & 0.000 & 0.012 & 0.015 \\ 0.015 & -0.012 & 0.000 & -0.010 \\ -0.294 & -0.015 & 0.010 & 0.000 \end{pmatrix}, \quad (\text{C8})$$

where χ_{ID} and χ'_{ID} correspond to the process matrix for resonant and detuned subspaces, with $\text{Re}(\cdot)$ and $\text{Im}(\cdot)$ representing the real and imaginary components, respectively.

$$\text{Re}(\chi'_H) = \begin{pmatrix} 0.010 & -0.003 & 0.004 & 0.002 \\ -0.003 & 0.561 & -0.002 & 0.480 \\ 0.004 & -0.002 & 0.002 & -0.003 \\ 0.002 & 0.480 & -0.003 & 0.464 \end{pmatrix}, \quad (\text{C9})$$

APPENDIX C: EXPERIMENTAL RESULT FOR SIMULTANEOUS CONTROL

The data of the χ matrix in each of the subspaces are

$$\text{Re}(\chi'_S) = \begin{pmatrix} 0.547 & -0.003 & -0.049 & 0.000 \\ -0.000 & 0.012 & -0.000 & -0.002 \\ -0.049 & -0.000 & 0.020 & -0.000 \\ 0.000 & -0.002 & -0.000 & 0.460 \end{pmatrix}, \quad (\text{C1})$$

$$\text{Im}(\chi'_H) = \begin{pmatrix} 0.000 & -0.040 & 0.006 & 0.051 \\ 0.040 & 0.000 & 0.004 & -0.006 \\ -0.006 & -0.004 & 0.000 & 0.001 \\ -0.051 & 0.006 & -0.012 & 0.000 \end{pmatrix}, \quad (\text{C10})$$

$$\text{Im}(\chi'_S) = \begin{pmatrix} 0.000 & -0.035 & 0.003 & 0.491 \\ 0.035 & 0.000 & -0.006 & -0.003 \\ -0.003 & 0.006 & 0.000 & 0.008 \\ -0.491 & 0.003 & -0.007 & 0.000 \end{pmatrix}, \quad (\text{C2})$$

$$\text{Re}(\chi_H) = \begin{pmatrix} 0.016 & -0.006 & -0.018 & -0.014 \\ -0.006 & 0.536 & 0.014 & 0.489 \\ -0.018 & 0.014 & -0.0172 & -0.006 \\ -0.014 & 0.489 & -0.006 & 0.470 \end{pmatrix}, \quad (\text{C11})$$

$$\text{Re}(\chi_S) = \begin{pmatrix} 0.540 & -0.020 & 0.017 & -0.003 \\ -0.020 & -0.016 & 0.003 & -0.025 \\ 0.017 & 0.003 & 0.030 & -0.020 \\ -0.003 & -0.025 & -0.020 & 0.475 \end{pmatrix}, \quad (\text{C3})$$

$$\text{Im}(\chi_H) = \begin{pmatrix} 0.000 & 0.008 & 0.018 & 0.069 \\ -0.008 & 0.000 & -0.010 & -0.018 \\ -0.018 & 0.010 & 0.000 & 0.007 \\ -0.069 & 0.018 & -0.007 & 0.000 \end{pmatrix}, \quad (\text{C12})$$

$$\text{Im}(\chi_S) = \begin{pmatrix} 0.000 & -0.001 & -0.018 & 0.487 \\ 0.001 & 0.000 & 0.037 & 0.018 \\ 0.018 & -0.037 & 0.000 & 0.008 \\ -0.487 & -0.018 & -0.008 & 0.000 \end{pmatrix}, \quad (\text{C4})$$

where $\chi_{S/T/H}$ and $\chi'_{S/T/H}$ correspond to the simultaneous S , T , and H gates process matrix for resonant and detuned spaces, with $\text{Re}(\cdot)$ and $\text{Im}(\cdot)$ representing the real and imaginary components, respectively.

[1] J. R. Kuklinski, U. Gaubatz, F. T. Hioe, and K. Bergmann, Adiabatic population transfer in a three-level system driven by delayed laser pulses, *Phys. Rev. A* **40**, 6741(R) (1989).

- [2] K. Bergmann, H. Theuer, and B. W. Shore, Coherent population transfer among quantum states of atoms and molecules, *Rev. Mod. Phys.* **70**, 1003 (1998).
- [3] N. V. Vitanov, A. A. Rangelov, B. W. Shore, and K. Bergmann, Stimulated Raman adiabatic passage in physics, chemistry, and beyond, *Rev. Mod. Phys.* **89**, 015006 (2017).
- [4] R. G. Unanyan and M. Fleischhauer, Geometric phase gate without dynamical phases, *Phys. Rev. A* **69**, 050302(R) (2004).
- [5] D. Møller, J. L. Sørensen, J. B. Thomsen, and M. Drewsen, Efficient qubit detection using alkaline-earth-metal ions and a double stimulated Raman adiabatic process, *Phys. Rev. A* **76**, 062321 (2007).
- [6] B. Rousseaux, S. Guérin, and N. V. Vitanov, Arbitrary qudit gates by adiabatic passage, *Phys. Rev. A* **87**, 032328 (2013).
- [7] I. Paparelle, L. Moro, and E. Prati, Digitally stimulated Raman passage by deep reinforcement learning, *Phys. Lett. A* **384**, 126266 (2020).
- [8] V. Giovannetti, S. Lloyd, and L. Maccone, Quantum-enhanced measurements: Beating the standard quantum limit, *Science* **306**, 1330 (2004).
- [9] A. Blais, A. L. Grimsmo, S. M. Girvin, and A. Wallraff, Circuit quantum electrodynamics, *Rev. Mod. Phys.* **93**, 025005 (2021).
- [10] C. Monroe, W. C. Campbell, L.-M. Duan, Z.-X. Gong, A. V. Gorshkov, P. W. Hess, R. Islam, K. Kim, N. M. Linke, G. Pagano, P. Richerme, C. Senko, and N. Y. Yao, Programmable quantum simulations of spin systems with trapped ions, *Rev. Mod. Phys.* **93**, 025001 (2021).
- [11] L. M. K. Vandersypen and I. L. Chuang, NMR techniques for quantum control and computation, *Rev. Mod. Phys.* **76**, 1037 (2005).
- [12] C. J. Ballance, T. P. Harty, N. M. Linke, M. A. Sepiol, and D. M. Lucas, High-Fidelity Quantum Logic Gates Using Trapped-Ion Hyperfine Qubits, *Phys. Rev. Lett.* **117**, 060504 (2016).
- [13] C.-w. Chou, C. Kurz, D. B. Hume, P. N. Plessow, D. R. Leibbrandt, and D. Leibfried, Preparation and coherent manipulation of pure quantum states of a single molecular ion, *Nature (London)* **545**, 203 (2017).
- [14] J. P. Gaebler, T. R. Tan, Y. Lin, Y. Wan, R. Bowler, A. C. Keith, S. Glancy, K. Coakley, E. Knill, D. Leibfried, and D. J. Wineland, High-Fidelity Universal Gate Set for $^9\text{Be}^+$ Ion Qubits, *Phys. Rev. Lett.* **117**, 060505 (2016).
- [15] Y. Lin, D. R. Leibbrandt, D. Leibfried, and C.-W. Chou, Quantum entanglement between an atom and a molecule, *Nature* **581**, 273 (2020).
- [16] D. Hayes, D. Stack, B. Bjork, A. C. Potter, C. H. Baldwin, and R. P. Stutz, Eliminating Leakage Errors in Hyperfine Qubits, *Phys. Rev. Lett.* **124**, 170501 (2020).
- [17] J. Li, J. Cui, R. Laflamme, and X. Peng, Selective-pulse-network compilation on a liquid-state nuclear-magnetic-resonance system, *Phys. Rev. A* **94**, 032316 (2016).
- [18] N. Khaneja, T. Reiss, C. Kehlet, T. Schulte-Herbrüggen, and S. J. Glaser, Optimal control of coupled spin dynamics: design of NMR pulse sequences by gradient ascent algorithms, *J. Magn. Reson.* **172**, 296 (2005).
- [19] A. M. Forney, S. R. Jackson, and F. W. Strauch, Multifrequency control pulses for multilevel superconducting quantum circuits, *Phys. Rev. A* **81**, 012306 (2010).
- [20] P. Rebentrost and F. K. Wilhelm, Optimal control of a leaking qubit, *Phys. Rev. B* **79**, 060507(R) (2009).
- [21] D. J. Egger and F. K. Wilhelm, Adaptive Hybrid Optimal Quantum Control for Imprecisely Characterized Systems, *Phys. Rev. Lett.* **112**, 240503 (2014).
- [22] F. Dolde, V. Bergholm, Y. Wang, I. Jakobi, B. Naydenov, S. Pezzagna, J. Meijer, F. Jelezko, P. Neumann, T. Schulte-Herbrüggen, J. Biamonte, and J. Wrachtrup, High-fidelity spin entanglement using optimal control, *Nat. Commun.* **5**, 3371 (2014).
- [23] M. Jiang, J. Bian, X. Liu, H. Wang, Y. Ji, B. Zhang, X. Peng, and J. Du, Numerical optimal control of spin systems at zero magnetic field, *Phys. Rev. A* **97**, 062118 (2018).
- [24] J. Tian, H. Liu, Y. Liu, P. Yang, R. Betzholz, R. S. Said, F. Jelezko, and J. Cai, Quantum optimal control using phase-modulated driving fields, *Phys. Rev. A* **102**, 043707 (2020).
- [25] S. Kirchhoff, T. Keßler, P. J. Liebermann, E. Assémat, S. Machnes, F. Motzoi, and F. K. Wilhelm, Optimized cross-resonance gate for coupled transmon systems, *Phys. Rev. A* **97**, 042348 (2018).
- [26] V. M. Schäfer, C. J. Ballance, K. Thirumalai, L. J. Stephenson, T. G. Ballance, A. M. Steane, and D. M. Lucas, Fast quantum logic gates with trapped-ion qubits, *Nature* **555**, 75 (2018).
- [27] R. Schutjens, F. A. Dagga, D. J. Egger, and F. K. Wilhelm, Single-qubit gates in frequency-crowded transmon systems, *Phys. Rev. A* **88**, 052330 (2013).
- [28] L. S. Theis, F. Motzoi, and F. K. Wilhelm, Simultaneous gates in frequency-crowded multilevel systems using fast, robust, analytic control shapes, *Phys. Rev. A* **93**, 012324 (2016).
- [29] Z. Chen, *et al.*, Measuring and Suppressing Quantum State Leakage in a Superconducting Qubit, *Phys. Rev. Lett.* **116**, 020501 (2016).
- [30] L. S. Theis, F. Motzoi, S. Machnes, and F. K. Wilhelm, Counteracting systems of diabaticities using DRAG controls: The status after 10 years, *EPL* **123**, 60001 (2018).
- [31] E. Barnes and S. Das Sarma, Analytically Solvable Driven Time-Dependent Two-Level Quantum Systems, *Phys. Rev. Lett.* **109**, 060401 (2012).
- [32] E. Barnes, Analytically solvable two-level quantum systems and Landau-Zener interferometry, *Phys. Rev. A* **88**, 013818 (2013).
- [33] S. E. Economou and E. Barnes, Analytical approach to swift nonleaky entangling gates in superconducting qubits, *Phys. Rev. B* **91**, 161405(R) (2015).
- [34] S.-L. Zhu, C. Monroe, and L.-M. Duan, Trapped Ion Quantum Computation with Transverse Phonon Modes, *Phys. Rev. Lett.* **97**, 050505 (2006).
- [35] M. J. Peterer, S. J. Bader, X. Jin, F. Yan, A. Kamal, T. J. Gudmundsen, P. J. Leek, T. P. Orlando, W. D. Oliver, and S. Gustavsson, Coherence and Decay of Higher Energy Levels of a Superconducting Transmon Qubit, *Phys. Rev. Lett.* **114**, 010501 (2015).
- [36] J. Randall, A. M. Lawrence, S. C. Webster, S. Weidt, N. V. Vitanov, and W. K. Hensinger, Generation of high-fidelity quantum control methods for multilevel systems, *Phys. Rev. A* **98**, 043414 (2018).

- [37] P. J. Low, B. M. White, A. A. Cox, M. L. Day, and C. Senko, Practical trapped-ion protocols for universal qudit-based quantum computing, *Phys. Rev. Res.* **2**, 033128 (2020).
- [38] Y. Wang, Z. Hu, B. C. Sanders, and S. Kais, Qudits and high-dimensional quantum computing, *Front. Phys.* **8**, 589504 (2020).
- [39] M. Ringbauer, M. Meth, L. Postler, R. Stricker, R. Blatt, P. Schindler, and T. Monz, A universal qudit quantum processor with trapped ions, *Nat. Phys.* **18**, 1053 (2022).
- [40] Q.-X. Mei, B.-W. Li, Y.-K. Wu, M.-L. Cai, Y. Wang, L. Yao, Z.-C. Zhou, and L.-M. Duan, Experimental Realization of the Rabi-Hubbard Model with Trapped Ions, *Phys. Rev. Lett.* **128**, 160504 (2022).
- [41] D. Leibfried, R. Blatt, C. Monroe, and D. Wineland, Quantum dynamics of single trapped ions, *Rev. Mod. Phys.* **75**, 281 (2003).
- [42] A. R. Conn, N. I. M. Gould, and P. L. Toint, *Trust Region Methods* (Society for Industrial and Applied Mathematics, Philadelphia, PA, USA, 2000).
- [43] A. C. Keith, C. H. Baldwin, S. Glancy, and E. Knill, Joint quantum-state and measurement tomography with incomplete measurements, *Phys. Rev. A* **98**, 042318 (2018).
- [44] C. R. Clark, H. N. Tinkey, B. C. Sawyer, A. M. Meier, K. A. Burkhardt, C. M. Seck, C. M. Shappert, N. D. Guise, C. E. Volin, S. D. Fallek, H. T. Hayden, W. G. Rellergert, and K. R. Brown, High-Fidelity Bell-State Preparation with $^{40}\text{Ca}^+$ Optical Qubits, *Phys. Rev. Lett.* **127**, 130505 (2021).
- [45] J. Zhang, A. M. Souza, F. D. Brandao, and D. Suter, Protected Quantum Computing: Interleaving Gate Operations with Dynamical Decoupling Sequences, *Phys. Rev. Lett.* **112**, 050502 (2014).
- [46] M. Riebe, K. Kim, P. Schindler, T. Monz, P. O. Schmidt, T. K. Körber, W. Hänsel, H. Häffner, C. F. Roos, and R. Blatt, Process Tomography of Ion Trap Quantum Gates, *Phys. Rev. Lett.* **97**, 220407 (2006).
- [47] M. A. Nielsen and I. L. Chuang, *Quantum Computation and Quantum Information: 10th Anniversary Edition* (Cambridge University Press, New York, USA, 2010).
- [48] X. Wang, C.-S. Yu, and X. X. Yi, An alternative quantum fidelity for mixed states of qudits, *Phys. Lett. A* **373**, 58 (2008).
- [49] A. Soare, H. Ball, D. Hayes, J. Sastrawan, M. C. Jarratt, J. J. McLoughlin, X. Zhen, T. J. Green, and M. J. Biercuk, Experimental noise filtering by quantum control, *Nat. Phys.* **10**, 825 (2014).
- [50] P. Wang, Z. Yuan, P. Huang, X. Rong, M. Wang, X. Xu, C. Duan, C. Ju, F. Shi, and J. Du, High-resolution vector microwave magnetometry based on solid-state spins in diamond, *Nat. Commun.* **6**, 6631 (2015).
- [51] C. Langer, Ph.D. thesis, University of Colorado, Boulder, 2006.